

Mass-asymmetric fission of $^{205,207,209}\text{Bi}$ at energies close to the fission barrier using proton bombardment of $^{204,206,208}\text{Pb}$

B. M. A. Swinton-Bland^{1,*}, M. A. Stoyer², A. C. Berriman¹, D. J. Hinde¹, C. Simenel^{1,3}, J. Buete¹, T. Tanaka¹, K. Banerjee^{1,†}, L. T. Bezzina¹, I. P. Carter¹, K. J. Cook^{1,‡}, M. Dasgupta¹, D. Y. Jeung¹, C. Sengupta^{1,§}, E. C. Simpson¹, and K. Vo-Phuoc¹

¹*Department of Nuclear Physics, Research School of Physics, Australian National University, Canberra, ACT 2601, Australia*

²*Nuclear Chemical Sciences Division, Lawrence Livermore National Laboratory, Livermore, California 94550, USA*

³*Department of Theoretical Physics, Research School of Physics, Australian National University, Canberra, ACT 2601, Australia*



(Received 4 September 2020; accepted 22 October 2020; published 24 November 2020)

Background: Recent observation of mass-asymmetric fission in neutron-deficient Hg and Pt nuclei has reignited interest in fission fragment mass distributions close to Pb. Investigations at energies close to the fission barrier, where mass-asymmetric fission is expected to be most obvious and the sensitivity to shell effects is maximized, are limited in this mass region.

Purpose: To measure fission mass distributions for $^{205,207,209}\text{Bi}$ nuclei at the lowest possible excitation energies to determine how the mass distributions change with excitation energy and the neutron number of the compound nucleus.

Method: Proton beams bombarding targets of $^{204,206,208}\text{Pb}$ were used to study the fission of $^{205,207,209}\text{Bi}$ at energies from just above to 10 MeV above their fission barriers. Fission fragments were measured using the CUBE fission spectrometer. Fission fragment mass distributions were determined using a newly developed time difference analysis method. Mass distributions were characterized by triple-Gaussian fits to determine the systematic trends across each isotope with excitation energy.

Results: Measured mass distributions of all three Bi isotopes exhibit a component of mass-asymmetric fission at all energies studied. The probability of mass-asymmetric fission decreases significantly with increasing excitation energy, from ≈ 70 to $\approx 40\%$ over a 10-MeV range. Comparisons between the three Bi isotopes hint at an increase in the mass-symmetric fission yield with increasing neutron number, which could be due to a decrease in the difference between the symmetric and asymmetric fission barriers. The centroids of the mass-asymmetric peaks suggest that several deformed shell gaps in the fission fragments could be contributing to the presence of the mass-asymmetric fission mode with $Z_{\text{light}} \simeq 38$, $Z_{\text{heavy}} \simeq 45$, and $N_{\text{light}} \simeq 56$ all present in the fission fragments.

Conclusions: Measurements of fission mass distributions at the lowest possible excitation energies above the fission barrier provide an excellent platform to investigate the origins of the mass-asymmetric fission mode. Further systematic measurements at these energies offer an opportunity to rigorously test new models of fission in this mass region.

DOI: [10.1103/PhysRevC.102.054611](https://doi.org/10.1103/PhysRevC.102.054611)

I. INTRODUCTION

Since the discovery of nuclear fission in 1939 [1,2], a complete understanding of this complex process has yet to be reached, and is currently the subject of active debate [3,4]. Originally fission was described by the macroscopic liquid drop model [5,6], which predicted that the lowest fission

barriers are found for symmetric mass splits. However, the observation of mass-asymmetric fission in actinide nuclei indicated that nuclear structure effects are important [7]. Initially the mass asymmetry was attributed to strong shell effects in the fission fragments, in particular the spherical magic numbers $N = 82$ and $Z = 50$ present in $^{132}\text{Sn}_{82}$. However, a systematic study of fission of actinide nuclei found that the dominant mass-asymmetric standard I and standard II fission modes are located around $Z = 52.5$ and 55 , respectively [8,9]. It was recently proposed that shell gaps for octupole deformations at $Z = 52$ and 56 may be responsible for the mass-asymmetric fission of actinide nuclei, by providing stability to the fission fragments as they undergo elongation during the fission process [10].

Modern experiments have expanded the region of mass-asymmetric fission to neutron-deficient Hg and Pt nuclei

*Corresponding author: ben.swinton-bland@anu.edu.au

[†]Present address: Variable Energy Cyclotron Centre, 1/AF, Bidhan Nagar, Kolkata 700064, India.

[‡]Present address: National Superconducting Cyclotron Laboratory, Michigan State University, East Lansing, MI 48824, USA.

[§]Present address: ACRF Image X Institute, University of Sydney, Central Clinical School, Sydney, Australia.

[11,12]. In particular, the observation of mass-asymmetric fission in neutron-deficient ^{180}Hg was surprising, given that mass-symmetric fission resulting in two doubly magic ^{90}Zr fragments is energetically more favorable. Instead, the mass-asymmetric fission must originate from local structure of the fission potential-energy surface (PES) near the fission saddle point [11]. This too has been recently associated with octupole correlations, in this case with octupole deformed neutron shell gaps at $N = 52$ and 56 [13], suggesting the possible universality of mass-asymmetric fission being driven by octupole deformations of the fission fragments. In addition, proton shell gaps were found to be present for large quadrupole deformations at $Z = 34$ and $Z = 42, 44$, and 46 , which could also drive mass-asymmetric fission in this region [13].

Fission of nuclei between the neutron-deficient Hg/Pt region and the neutron-rich actinide nuclei was previously expected to be predominantly mass symmetric, though some notable exceptions have been reported in the literature. For example, mass-asymmetric fission was observed in ^{201}Tl [14] at an excitation energy of ≈ 7 MeV above the saddle-point energy. Furthermore, an indication of mass-asymmetric fission in both ^{205}Bi [15] and ^{207}Bi [16] at energies down to ≈ 10 MeV above the saddle point has also been reported.

To investigate mass-asymmetric fission in this mass region—and to maximize the sensitivity to shell effects—systematic measurements at the lowest possible excitation energies above the fission barrier are required. Here, we present measurements of fission fragment mass distributions of $^{205,207,209}\text{Bi}$ at excitation energies ranging from just above the fission barrier to ≈ 10 MeV above. This allows investigation of the dependence of the mass distributions on both excitation energy and neutron number of the fissioning nucleus.

This paper is structured as follows: Experimental details are presented in Sec. II, including a full description of the newly developed time difference analysis method used in this work. A discussion of the characteristics of the fission fragment mass distributions is presented in Sec. III, along with comparisons to model calculations. Conclusions and future work are then discussed in Sec. IV.

II. EXPERIMENTAL DETAILS

Proton beams were delivered by the 14UD tandem electrostatic accelerator at the Australian National University Heavy Ion Accelerator Facility. A dc beam was used to maximize the beam current and therefore the fission rate. The targets used for these experiments are detailed in Table I.

Beam energies ranged from 18.99 to 28.00 MeV, with the beam energy known to better than 0.1% [17]. The resultant excitation energies, E_x , and the excitation energies above the calculated fission barriers, B_{fis} (from Möller *et al.* [18]), are shown in Table II for each of the reactions studied. Excitation energies varied from just above to ≈ 10 MeV above the calculated B_{fis} .

Fission fragments were detected using the CUBE fission spectrometer [19–21], configured here with two large area (279×357 -mm active area) position sensitive multiwire proportional counters (MWPCs). The detectors were placed

TABLE I. Target specifications used in this experiment determined from elastic-scattering measurements of ^{16}O on the four targets and reference targets of ^{197}Au of known thicknesses.

Target	Target thickness ($\mu\text{g}/\text{cm}^2$)	Backing material	Backing thickness ($\mu\text{g}/\text{cm}^2$)
^{204}PbS	54	$^{\text{nat}}\text{C}$	23
^{206}PbS	211	$^{\text{nat}}\text{C}$	33
^{208}PbS	213	$^{\text{nat}}\text{C}$	33
$^{204}\text{Pb}^a$	600	$^{\text{nat}}\text{C}$	18

^aElemental target used for the $E_{\text{beam}} = 19$ MeV reaction.

180 mm from the target and covered scattering angles of approximately 5° – 80° in the forward direction and 95° – 170° in the backward direction. A schematic diagram of the detector configuration used in this experiment is given in Fig. 1(a) of Ref. [21], along with additional experimental details. The targets were angled at 45° with respect to the beam direction to minimize the energy loss of the fission fragments through the target. Target thicknesses were determined using separate in-beam elastic-scattering measurements of ^{16}O on the four targets, using reference targets of ^{197}Au of known thicknesses. Energy-loss corrections of mass-identified fission fragments traversing the target and/or the backing were applied iteratively event-by-event, assuming that the fission occurred at the center of the target.

With the use of a dc beam, the quantities available are the time difference between the two fission fragments and their positions and energy losses in the two MWPC detectors. The folding angle between the two fragments, both in the plane containing the beam, θ_{12} , and normal to the beam, ϕ_{12} , could be determined from the geometrical relationship between the target and the MWPCs. These variables allowed confirmation that events were back-to-back in the center-of-mass frame, validating the kinematic reconstruction of the binary fragments.

TABLE II. Reaction, energy of the proton beam, E_{beam} , compound nucleus excitation energy, E_x , and excitation energy with respect to the calculated Möller *et al.* [18] fission barrier, B_{fis} , for all measurements presented in this paper. The 19-MeV $p + ^{204}\text{Pb}$ reaction used the elemental target listed in Table I. The fission barrier heights for $^{205,207,209}\text{Bi}$ are 20.47, 22.28, and 23.88 MeV, respectively [18].

Reaction	E_{beam} (MeV)	E_x (MeV)	$E_x - B_{\text{fis}}$ (MeV)
$p + ^{204}\text{Pb}$	18.99	22.13	1.66
$p + ^{204}\text{PbS}$	20.99	24.13	3.66
$p + ^{206}\text{PbS}$	20.99	24.44	2.16
$p + ^{204}\text{PbS}$	22.98	26.11	5.64
$p + ^{206}\text{PbS}$	22.98	26.42	4.14
$p + ^{204}\text{PbS}$	24.99	28.10	7.63
$p + ^{206}\text{PbS}$	24.98	28.42	6.14
$p + ^{208}\text{PbS}$	24.98	28.66	4.78
$p + ^{204}\text{PbS}$	28.00	31.10	10.63
$p + ^{206}\text{PbS}$	28.00	31.42	9.14
$p + ^{208}\text{PbS}$	28.00	31.66	7.78

The fission mass split has previously been determined from the time difference and flight path information in heavy-ion induced fission. Typically, the center-of-mass velocity, v_{cm} , is known and is a significant fraction of the fission fragment velocity. Through the resultant change in folding angle θ_{12} with total kinetic energy (TKE), both the fission mass split and TKE can be determined [19,22–24].

Unlike heavy-ion induced fission, θ_{12} in fission induced through proton bombardment reactions is close to 180° , and is spread by neutron evaporation and angular straggling in the target. This results in the deduced TKE and fragment velocities having extremely poor resolution, leading to very poor mass resolution. This issue has been overcome through a development of the time difference analysis method as described below.

A. Determining fission fragment masses using time difference

The determination of fragment masses (m_1, m_2) through the time difference between the two fission fragments is based on momentum conservation after scission. For asymptotic fragment velocities, with magnitude $v_{\text{cm}(1)}$ and $v_{\text{cm}(2)}$, this means $m_1 v_{\text{cm}(1)} = m_2 v_{\text{cm}(2)}$. From a single observable (time difference) it is not possible to independently determine the two fragment masses. Instead, the mass ratio, M_R , at scission can be determined by [20]

$$M_R = \frac{m_1}{m_1 + m_2} = \frac{v_{\text{cm}(2)}}{v_{\text{cm}(1)} + v_{\text{cm}(2)}}, \quad (1)$$

where m_1 and m_2 are the masses of the two fission fragments. Assuming no pre-scission particle emission (a safe assumption for reactions with excitation energies typically < 8 MeV above the fission barrier), fragment masses at scission are given in terms of the mass of the fissioning compound nucleus A_{CN} , namely, $m_1 = M_R A_{\text{CN}}$ and $m_2 = (1 - M_R) A_{\text{CN}}$.

The measured time difference, Δt , can be expressed as

$$\Delta t = \frac{d_2}{v_2} - \frac{d_1}{v_1}, \quad (2)$$

where $d_{1,2}$ are the distances from the target to the detector that each fragment traverses and $v_{1,2}$ are the calculated velocities of the fragments. Where the time difference Δt is nonzero, the absolute fission fragment velocities are required, which are not measured. However, the sum of the average fragment velocities in the center-of-mass frame, $K = v_{\text{cm}(1)} + v_{\text{cm}(2)}$, can be shown to be almost independent of the mass split, and takes values close to 2.4 cm/ns [25,26]. Fragment velocities can then be expressed in terms of M_R and K such that $v_{\text{cm}(1)} = (1 - M_R)K$ and $v_{\text{cm}(2)} = M_R K$.

The fragment velocities in the laboratory frame are required in Eq. (2). For $v_{\text{CN}} \ll v_{\text{cm}(i)}$ (where v_{CN} is the compound nucleus velocity), we can approximate the laboratory frame velocities as

$$v_i = v_{\text{cm}(i)} + v_{\text{CN}} \cos \theta_i, \quad (3)$$

resulting in

$$v_1 \simeq (1 - M_R)K + v_{\text{CN}} \cos \theta_1, \quad (4)$$

$$v_2 \simeq M_R K + v_{\text{CN}} \cos \theta_2. \quad (5)$$

We take v_{CN} to be that for complete momentum transfer in fusion. This is a good assumption here, since any momentum that might be carried away by a preequilibrium particle will reduce the excitation energy of the compound nucleus, and thus drastically suppress the fission probability.

Substituting Eqs. (4) and (5) into Eq. (2) and dropping terms in $(v_{\text{CN}})^2$ results in an expression for the time difference that is quadratic in M_R :

$$\Delta t = \frac{d_2[(1 - M_R)K + v_{\text{CN}} \cos \theta_1] - d_1[M_R K + v_{\text{CN}} \cos \theta_2]}{[M_R K + v_{\text{CN}} \cos \theta_2][(1 - M_R)K + v_{\text{CN}} \cos \theta_1]}. \quad (6)$$

Equation (6) can be rearranged to give

$$aM_R^2 + bM_R + c = 0, \quad (7)$$

where

$$a = -K \Delta t, \quad (8)$$

$$b = K \Delta t + (d_1 + d_2) + \Delta t v_{\text{CN}} (\cos \theta_1 - \cos \theta_2), \quad (9)$$

$$c = -d_2 + v_{\text{CN}} \left[\Delta t \cos \theta_2 - \frac{1}{K} (d_2 \cos \theta_1 - d_1 \cos \theta_2) \right]. \quad (10)$$

M_R can therefore be written as the positive root of the quadratic equation and is expressed completely in terms of measured quantities and the calculated quantities v_{CN} and K that can be determined for the specific reaction. In this paper, K was calculated as a function of mass split [22] using the 1985 Viola TKE systematics [27]. The effect of uncertainty in the value of K can be simply evaluated using the approximate expression for M_R , taking $v_{\text{CN}} = 0$ and $d_1 = d_2 = d$ (true in this measurement) given by

$$M_R = 0.5 - \frac{K \Delta t}{8d}. \quad (11)$$

An uncertainty in TKE of 5% therefore corresponds to a 2.5% uncertainty in K . For a typical M_R of 0.47, this results in a change in M_R by less than 10^{-3} , or 0.15 u, which is smaller than other experimental uncertainties. Using this time difference analysis method, fission fragment mass distributions were thus extracted for each reaction.

B. Actinide target impurities

The presence of the possible actinide contaminants U and Th in the targets was investigated by measuring the fission yield as a function of proton beam energy. This is defined as the number of fissions per μC of beam current and is presented in Fig. 1. The fission yields for $p + {}^{232}\text{Th}$ and $p + {}^{238}\text{U}$ were also measured and are shown in Fig. 1, with both increasing slowly over the range of beam energies studied. The 19-MeV $p + {}^{204}\text{Pb}$ reaction used a thick elemental target, and the fission yield for this target was normalized to the thickness of the ${}^{204}\text{PbS}$ target. If the targets had no actinide contamination, the fission yield should decrease exponentially with beam energy, in line with the fission cross section. This is observed for the ${}^{204,206}\text{PbS}$ targets. However, the fission yield for the ${}^{208}\text{PbS}$ target saturates at the lowest beam energy measured, suggesting the presence of a level of actinide

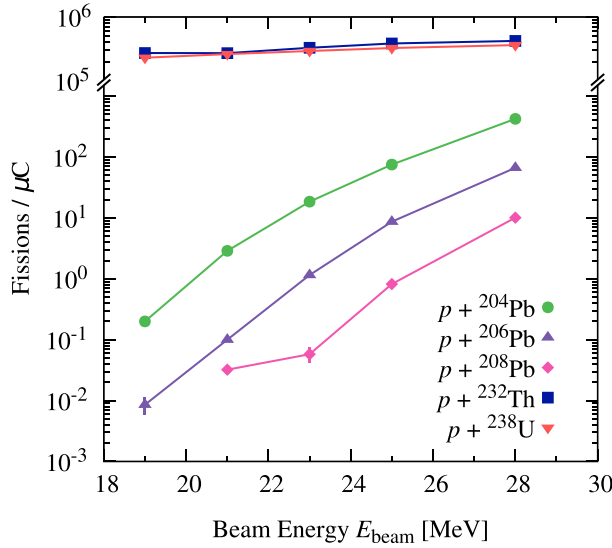


FIG. 1. Observed fission yield, defined as the number of fissions per μC of beam current, as a function of beam energy, E_{beam} , for the $p + {}^{204,206,208}\text{Pb}$, $p + {}^{232}\text{Th}$, and $p + {}^{238}\text{U}$ reactions. Lines are used to guide the eye. The y axis is split, with the fission yield for $p + {}^{232}\text{Th}$ and $p + {}^{238}\text{U}$ being at least three orders of magnitude larger than the $p + {}^{204,206,208}\text{Pb}$ fission yield at the same E_{beam} . Target contamination with fissionable contaminants such as U or Th would be evident at the lowest beam energies and appears to be negligible except for the ${}^{208}\text{Pb}$ data, which show a saturation of the fission yield for the lowest beam energy, which may be an indication of fissionable contaminants at an extremely low level present in the ${}^{208}\text{PbS}$ target.

contamination in this target. Based on the relative target thicknesses, the actinide impurity levels were estimated to be between 10 and 100 ppb (10^{-8} to 10^{-7}). We are therefore left with a question: does this low level of actinide contamination affect the measured fission mass distributions for ${}^{205,207,209}\text{Bi}$?

To answer this question, the mass ratio spectrum for the $p + {}^{208}\text{Pb}$ reaction at $E_{\text{beam}} = 25\text{ MeV}$ is shown in Fig. 2(a). Lower energies for the $p + {}^{208}\text{Pb}$ reaction showed evidence of impurities in the mass ratio spectra. The $p + {}^{232}\text{Th}$ and $p + {}^{238}\text{U}$ mass ratio distributions at $E_{\text{beam}} = 25\text{ MeV}$ are represented by the filled in points in Fig. 2(b). It is clear that the level of actinide contamination is very low, as there is a negligible yield outside of the range $0.4 < M_R < 0.6$, with the peak yields for the $p + {}^{232}\text{Th}$ or $p + {}^{238}\text{U}$ reactions situated at much more extreme M_R compared to the $p + {}^{208}\text{Pb}$ reaction.

Despite the observed lack of saturation for the $p + {}^{204}\text{Pb}$ reaction in Fig. 1, at the lowest measured energy, the fission yield cannot guarantee the absence of Th or U. Therefore, the mass ratio distribution for the $p + {}^{204}\text{Pb}$ reaction at $E_{\text{beam}} = 19\text{ MeV}$ is presented in Fig. 2(c), and the $p + {}^{232}\text{Th}$ and $p + {}^{238}\text{U}$ mass ratio distributions at $E_{\text{beam}} = 19\text{ MeV}$ are given in panel (b) by the hollow points. Here too the contribution from ${}^{232}\text{Th}$ or ${}^{238}\text{U}$ is clearly very small. We can therefore conclude that the general behavior of the measured fission mass distributions for the $p + {}^{204,206,208}\text{Pb}$ reactions is unaffected by low levels of actinide contamination in the targets.

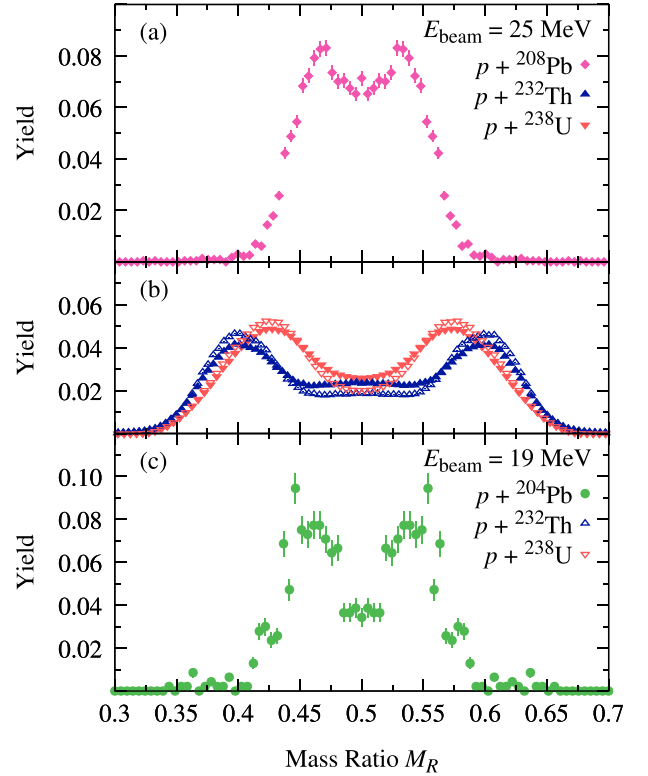


FIG. 2. Panels (a) and (c) show the fission mass ratio, M_R , distributions for $p + {}^{208}\text{Pb}$ at $E_{\text{beam}} = 25\text{ MeV}$ and $p + {}^{204}\text{Pb}$ at $E_{\text{beam}} = 19\text{ MeV}$. Panel (b) presents the fission M_R distributions for both $p + {}^{232}\text{Th}$ and $p + {}^{238}\text{U}$ reactions at 19 MeV (hollow points) and 25 MeV (solid points). No significant increase in yield is observed in panel (a) or (c) in the M_R region associated with either actinide, indicating that actinide contamination does not affect the fission mass distributions presented in this paper.

III. RESULTS AND DISCUSSION

All fission mass distributions were extracted from measured mass-angle distributions (MADs), which show the distribution of fission fragment mass ratio as a function of center-of-mass scattering angle, $\theta_{\text{c.m.}}$. The measured MADs are presented in Appendix A. Mass ratio spectra were obtained from the projection of the MAD onto the M_R axis. The MADs are mirrored about $M_R = 0.5$ and $\theta_{\text{c.m.}} = 90^\circ$, and thus the mass distributions are mirrored about mass symmetry. By binning the M_R spectra such that one bin represents one atomic mass unit, the M_R can be simply converted to atomic mass number A by taking the mass at scission to be that of the compound nucleus. Finally, the mass distribution yields are normalized to two fission fragments.

A. Comparison with previous work

Fission mass distributions for ${}^{205,207}\text{Bi}$ have been measured at energies $\approx 10\text{ MeV}$ above the saddle point by Itkis *et al.* [15,16]. These (digitally scanned) mass distributions are compared to the present measurements in Fig. 3, where there is a 0.5-MeV difference in excitation energy for ${}^{205}\text{Bi}$ and a 0.38-MeV difference for ${}^{207}\text{Bi}$. Therefore, comparisons

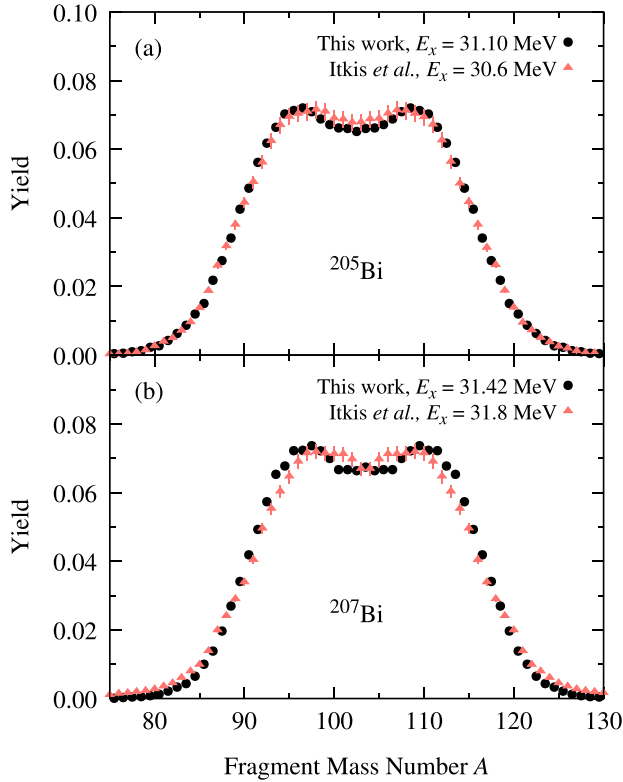


FIG. 3. Comparisons to the (digitally scanned) data from Itkis *et al.* for (a) ^{205}Bi [16] and (b) ^{207}Bi [15]. In the present experiment M_R has been converted to fragment mass number A . Both sets of mass distributions are normalized to two fission fragments. Overall the agreement is good, especially for the ^{205}Bi distribution, with both data sets showing the presence of a two-peak structure.

should focus on the general characteristics, rather than any extremely detailed differences between the mass distributions.

For ^{205}Bi , there is very good agreement between the two measurements, with both distributions having very similar widths and a double-peaked structure. For ^{207}Bi , the agreement is not quite as good, with the scanned mass distribution from Itkis *et al.* having a slightly wider base and the double-peaked structure being narrower. Even with these small differences, the mass distributions from Itkis *et al.* are well reproduced, highlighting the accuracy of the new time difference analysis method developed in this work.

B. Fission fragment mass distributions

The extracted fission fragment mass distributions for $^{205,207,209}\text{Bi}$ are presented in Figs. 4, 5, and 6, respectively. As can be seen, all three Bi isotopes exhibit a component of mass-asymmetric fission at all energies. With increasing excitation energy the relative yield at mass symmetry increases, demonstrated most clearly by ^{205}Bi in Fig. 4.

To quantify the change in shape of the mass distributions with excitation energy, double- and triple-Gaussian fits were performed on all fission mass distributions. The double-Gaussian fits, defined by two identical Gaussians that are

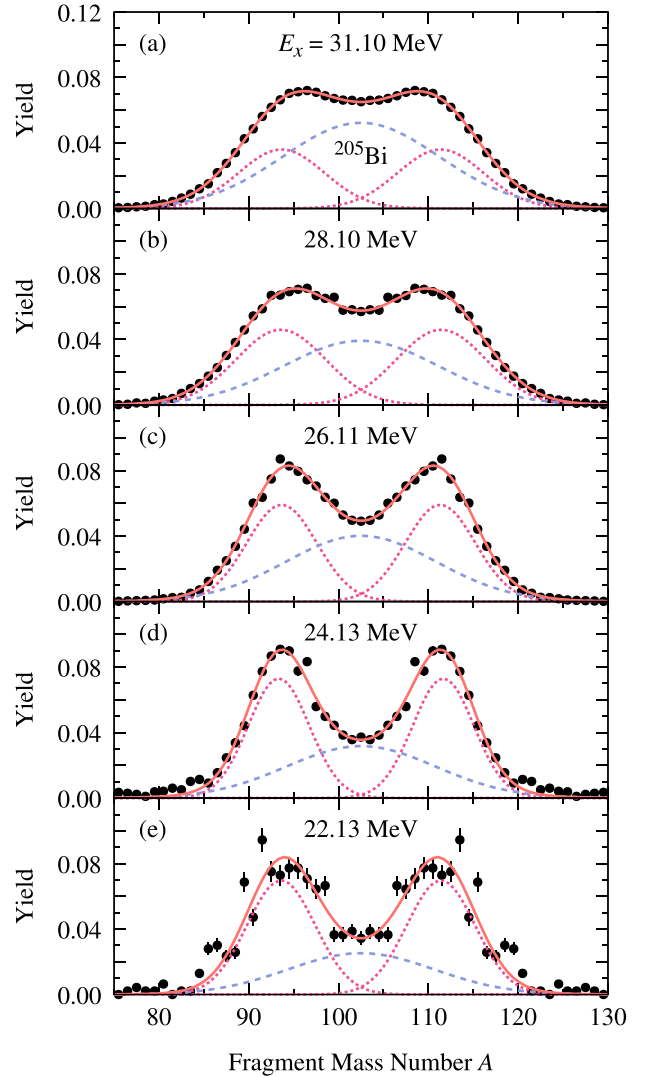


FIG. 4. Measured fission mass distributions for ^{205}Bi for five different excitation energies, E_x . As in Fig. 3, the mass distributions are normalized to two fission fragments and the mass ratio, M_R , has been converted to fragment mass number A . The triple-Gaussian fits (solid orange lines) are also shown, with the mass-symmetric component (light blue dashed line) and the mass-asymmetric component (pink dashed line) included. There is a clear increase in the mass-symmetric fission component with increasing excitation energy.

offset from mass symmetry by $\pm\Delta A$, consistently underestimated the yield of mass-symmetric fission, resulting in on average three times larger χ^2 values than the triple-Gaussian fits. A comparison between double- and triple-Gaussian fits is provided in Fig. 7(a), with residuals from the two fits shown in Fig. 7(b). It is clear that the double-Gaussian fit fails to match the data, especially at mass symmetry, resulting in the evident structure visible in the residuals plot which is absent for the triple-Gaussian fit. Furthermore, the error bars presented in Fig. 8, which shows the symmetric fission fraction as a function of excitation energy, highlight the statistical significance of the triple-Gaussian fits, with no error bars overlapping with

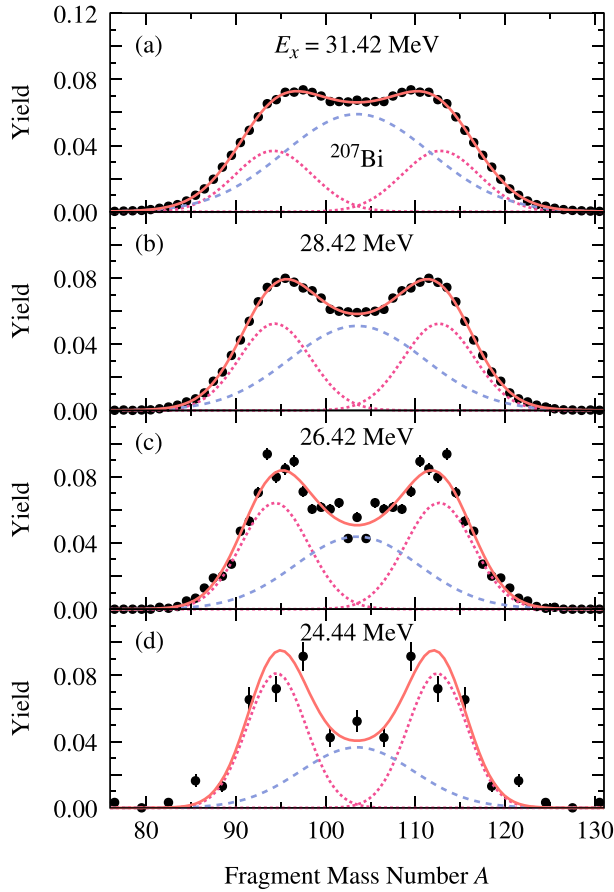


FIG. 5. As in Fig. 4 for ^{207}Bi fission at four different excitation energies, E_x . Panel (d) is binned in three mass unit bins, due to low statistics. Again, there is a gradual decrease in the mass-asymmetric component with increasing excitation energy.

an absence (zero symmetric fission fraction) of a symmetric fission component.

The triple-Gaussian fits added a Gaussian centered at mass symmetry. The common values of ΔA , height, and width of the mass-asymmetric Gaussians were unconstrained, as was the height of the mass-symmetric Gaussian. The width of the mass-symmetric Gaussian was also unconstrained in fitting the higher-energy distributions, but for the two lowest-energy $^{205,207}\text{Bi}$ and the lowest-energy ^{209}Bi mass distributions the symmetric mass widths had to be fixed, as the fits were increasingly unstable due to low statistics. The fixed mass widths were determined by extrapolating the mass widths determined from the higher-energy runs, and they follow a smooth increase with excitation energy, as would be expected. The triple-Gaussian fit parameters are presented in Table IV in Appendix B.

From the triple-Gaussian fits the fraction of mass-symmetric fission could be determined, and is presented as a function of excitation energy in Fig. 8. There is a clear increase in the symmetric fission fraction with increasing excitation energy for each Bi isotope. This trend could be due to a damping of shell effects responsible for the

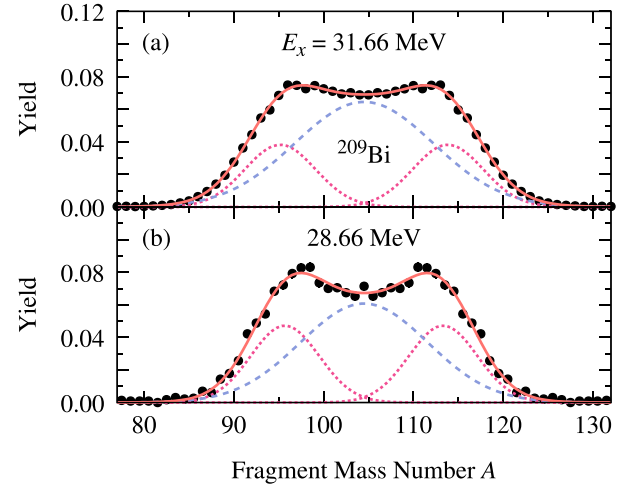


FIG. 6. As in Fig. 4 for ^{209}Bi fission at two different excitation energies, E_x . The increase in the mass-symmetric component with increasing excitation energy is again observed.

asymmetric mode, a phenomenon well known in the actinide region. However, theoretical calculations in the mercury region predict a small dependence of the potential-energy surface with excitation energy [28]. In addition, a recent study [29] found that at low excitation energies shell corrections depend weakly on excitation energy, in contrast with standard expectations [30].

Another interpretation of the increase in the symmetric fraction in Fig. 8 involves the relative heights between the saddle points for the symmetric and asymmetric fission modes. The dominance of the asymmetric mode at low excitation energy suggests that the barrier for this mode is lower than for symmetric fission. However, with increasing energy, the two modes are expected to trend towards equal weight. This scenario is supported by hints of evolution of the symmetric to asymmetric ratio with increasing neutron number of the compound nucleus, N_{CN} . This is suggested by the increased symmetric fission fraction for ^{209}Bi compared to ^{205}Bi in the two gray boxes labeled A and B in Fig. 8. Theoretical predictions of the fission barriers in $^{205,207,209}\text{Bi}$ [18] show an increase with neutron number (arrows in Fig. 8). Assuming a higher barrier for the symmetric valley that does not vary significantly with N_{CN} , we thus expect an increase of the symmetric fission yield with heavier Bi isotopes, in qualitative agreement with our experimental observation.

The centroids of the two mass-asymmetric Gaussians can also give information on the origin of the observed mass asymmetry. If we assume that the fission fragments will have the same N/Z ratio as the fissioning Bi isotope, following the unchanged-charge-density assumption [7], the neutron and proton numbers in the mass-asymmetric fragments can be determined ($Z_{\text{peak}} = A_{\text{peak}} \times \frac{Z_{\text{CN}}}{A_{\text{CN}}}$ and $N_{\text{peak}} = A_{\text{peak}} \times \frac{N_{\text{CN}}}{A_{\text{CN}}}$). These are presented as a function of excitation energy in Fig. 9. The centroids, within error, remain constant across the excitation energies studied, highlighting the stability of the triple-Gaussian fit peak positions. This also indicates

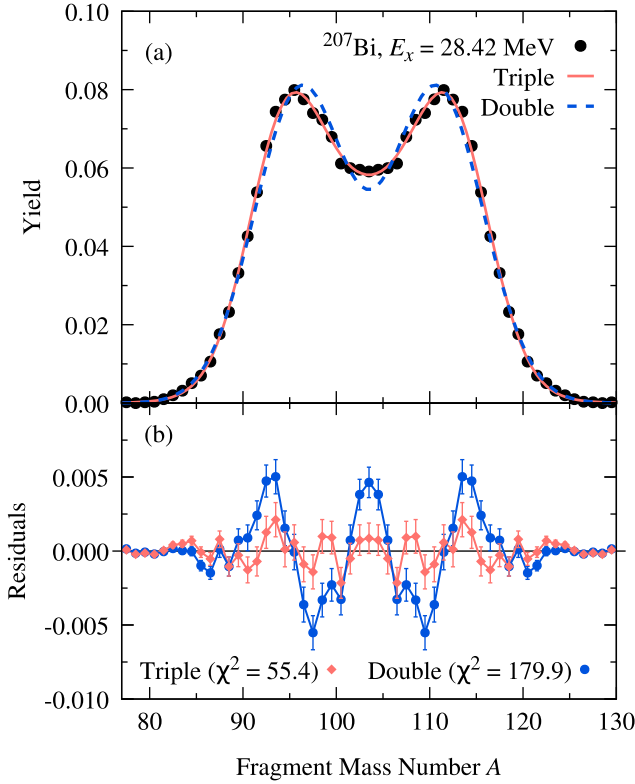


FIG. 7. (a) Double- and triple-Gaussian fits to the ^{207}Bi mass distribution at $E_x = 28.42$ MeV. Residuals are shown in panel (b); the lines guide the eye. The double-Gaussian fit cannot account for the yield at symmetry, which is clearly highlighted in the strong structure seen in the residual plot and the much larger (3.25 times) χ^2 value.

that the peak positions from the triple-Gaussian fits at all measured energies are directly related to the location of the mass-asymmetric fission valleys in the potential-energy surface.

The average centroid positions of each Bi isotope across all energies studied are presented in Table III. The proton numbers of both the light and heavy fission fragment remain constant across all three Bi isotopes in Fig. 9, with the light fragment having $Z_{\text{light}} \simeq 38$ and the heavy fragment having $Z_{\text{heavy}} \simeq 45$. Both of these proton numbers have recently been associated with mass-asymmetric fission in the sublead region. $Z = 45$ lies between two superdeformed quadrupole

TABLE III. Neutron and proton numbers of the light and heavy mass-asymmetric fission fragments determined from the average centroid position from the triple-Gaussian fits across all energies studied (see text).

Isotope	N_{light}	Z_{light}	N_{heavy}	Z_{heavy}
^{205}Bi	55.70(12)	37.90(8)	66.30(12)	45.10(8)
^{207}Bi	56.55(18)	37.85(12)	67.45(18)	45.15(12)
^{209}Bi	57.52(13)	37.90(9)	68.47(13)	45.10(9)

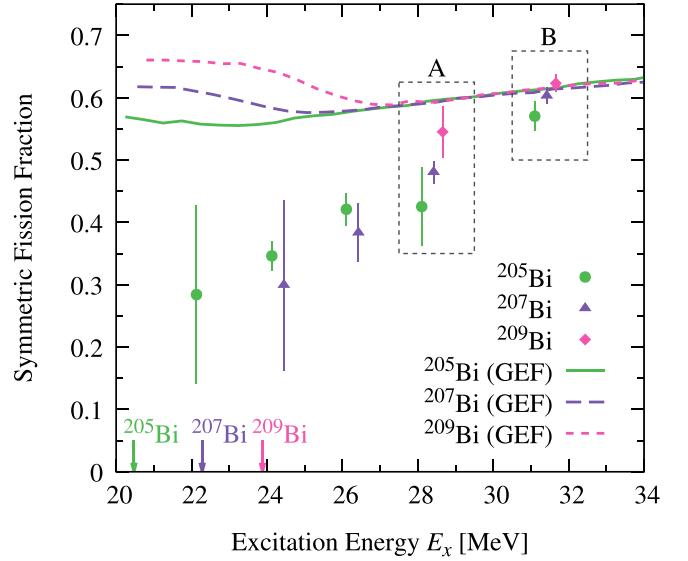


FIG. 8. Symmetric fission fraction, determined from the triple-Gaussian fits, as a function of excitation energy for all three Bi isotopes. GEF2019/1.3 calculations for each isotope are given by the colored lines, while the colored arrows represent the calculated Möller *et al.* [18] fission barrier, B_{fis} , for each Bi isotope. The gray boxes encompass the two different sets of data that are at similar excitation energies (see text). The significant increase in symmetric fission fraction with excitation energy is not present in the GEF calculations, which only show agreement at the highest measured energies, but considerably overpredict the symmetric fission fraction at the lowest energies.

shell gaps at $Z = 44$ and 46 [13,31] whereas a quadrupole shell gap at $Z = 38$ was found to be present when $N_{\text{light}} > 50$ from energy density-functional calculations when investigating the fission of ^{202}Pb [32]. In addition to these proton shell effects, the N_{light} values for all three Bi isotopes correlate with an octupole deformed shell gap at $N = 56$ [10]. With the presence of these three deformed shell effects in the mass-asymmetric fragments, it is difficult to make any definitive conclusions as to whether one of these effects may be the main driver of the observed mass-asymmetric fission in these Bi isotopes. Further systematic studies are required to determine which of these shell effects contribute.

C. Comparisons with theoretical models

The measured fission mass distributions for $^{205,207,209}\text{Bi}$ are compared with calculations from two models. These are the semiempirical General description of Fission observables (GEF2019/1.3) model [34], and a random-walk method on top of a phenomenological PES from Ref. [33].

1. GEF calculations

The GEF calculations include the standard I, standard II, and superasymmetric fission modes, all of which are mass asymmetric, and the superlong fission mode, which is mass

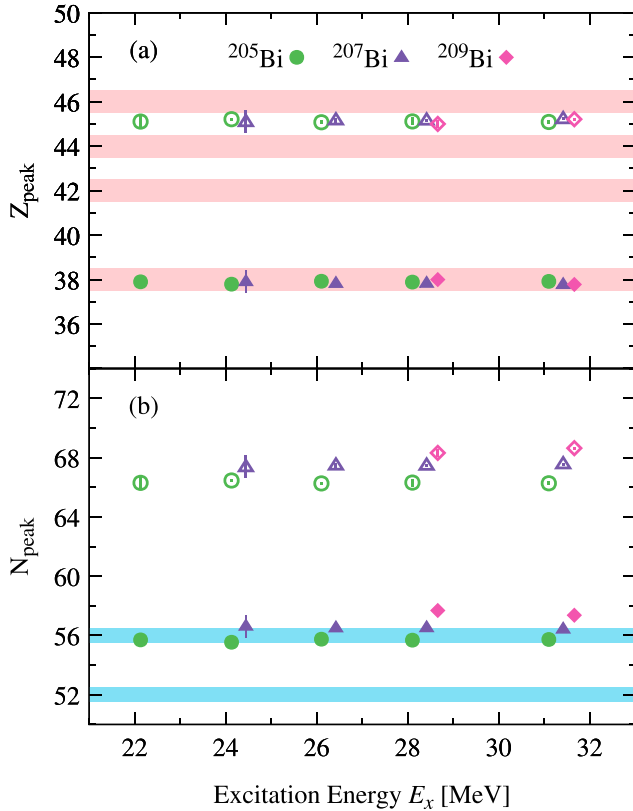


FIG. 9. Panel (a) shows light (solid points) and heavy (hollow points) fragment Z_{peak} values, determined from the triple-Gaussian fits, as a function of excitation energy for all three Bi isotopes, while panel (b) shows fragment N_{peak} as a function of excitation energy. Z_{peak} values in panel (a) correlate with expected quadrupole deformed proton shell gaps (pink bands) at $Z = 38$ for the light fragments and $Z = 44$ and 46 for the heavy fragments. The N_{peak} values lie close to $N = 56$ for the light fragments, where an octupole deformed neutron shell gap (blue band) is expected.

symmetric. An empirical mass-asymmetric fission mode centered around $Z \simeq 38$, but slightly varying with N to fit ^{180}Hg and ^{201}Tl experimental results, is also included.

For fission of the Bi isotopes studied, the two dominant fission modes determined by the GEF calculations are the superlong and the $Z \simeq 38$ mode, with the standard I and standard II modes contributing less than 1% typically. Thus, the calculated symmetric fission fraction is determined by the fraction of the superlong fission mode, and this is presented in Fig. 8. The GEF calculations show good agreement with experiment at the highest excitation energies in Fig. 8. However, they severely underestimate the reduction in the symmetric fission fraction with decreasing excitation energy that is seen experimentally. The disparity is highlighted in Figs. 10(a)–10(f), where the calculated fission fragment mass distributions from the GEF calculations for each isotope are compared to the measured distributions at two excitation energies. At low excitation energy the GEF calculations are substantially different from the data, most notably for ^{205}Bi in panel (a). The yield at mass symmetry is considerably larger in the GEF

calculations, which also show only minor changes between the different Bi isotopes and across the energy range. As GEF is a semiempirical model, this demonstrates the need for further measurements of fission fragment mass distributions at excitation energies close to the fission barrier.

2. Random-walk calculations over a potential-energy surface

Fission fragment yields for the Bi isotopes studied here have been calculated using a random-walk method on top of a phenomenological potential-energy surface in Ref. [33]. Five-dimensional potential-energy surfaces were calculated as described in [35] and include damping of microscopic effects with increasing excitation energy. Random walks from the ground-state minimum are performed on these surfaces to generate fission mass distributions. The random-walk method used was justified by the overdamped nature of fission, a conclusion supported by recent fully microscopic calculations [36].

Mass distributions can be compared at one excitation energy for $^{205,207,209}\text{Bi}$ fission as they are provided in the supplementary materials of Ref. [33]. These calculations have been digitally scanned and are compared to the mass distributions at the closest measured excitation energies in Figs. 10(d)–10(f). The excitation energies are similar for $^{205,207}\text{Bi}$, allowing direct comparisons to be made. However, the excitation energy for ^{209}Bi is significantly lower (2.55-MeV difference) than the random-walk calculation, and so comparisons should be tentative for this system.

The random-walk calculation reproduces the two-peaked structure present in the experimental data for ^{205}Bi [panel (d)]. For ^{207}Bi [panel (e)], it gives a slightly narrower mass distribution than the experiment. The measured fission mass distribution for ^{209}Bi [panel (f)] is similar to that for ^{207}Bi , with a dip at mass symmetry. In contrast, the calculated mass distribution is much narrower and strongly peaked at mass symmetry. This difference could in part be attributed to the significantly larger (2.55 MeV) excitation energy of the random-walk calculation.

As the random-walk calculations for these Bi isotopes are only given at one excitation energy, it is difficult to say if they would correctly predict the significant changes in the mass distributions with decreasing excitation energy. As can be seen in the GEF comparisons, it is at the lowest excitation energies where the disparity between the calculation and the experimental data is at its greatest. It is therefore crucial that future theoretical calculations are made at lower excitation energies, and that these calculations can correctly match the evolution of the mass distributions with increasing excitation energy.

As the competition between the mass-symmetric and mass-asymmetric modes may be due to the relative height of the saddle points (barriers) for the symmetric and asymmetric modes, the clearest way to investigate this competition is through the potential-energy surface that is used in theoretical calculations. Therefore, random-walk or time-dependent generator coordinate methods [37] based on fully microscopic potential-energy surfaces would be desirable to help further interpret the present data.

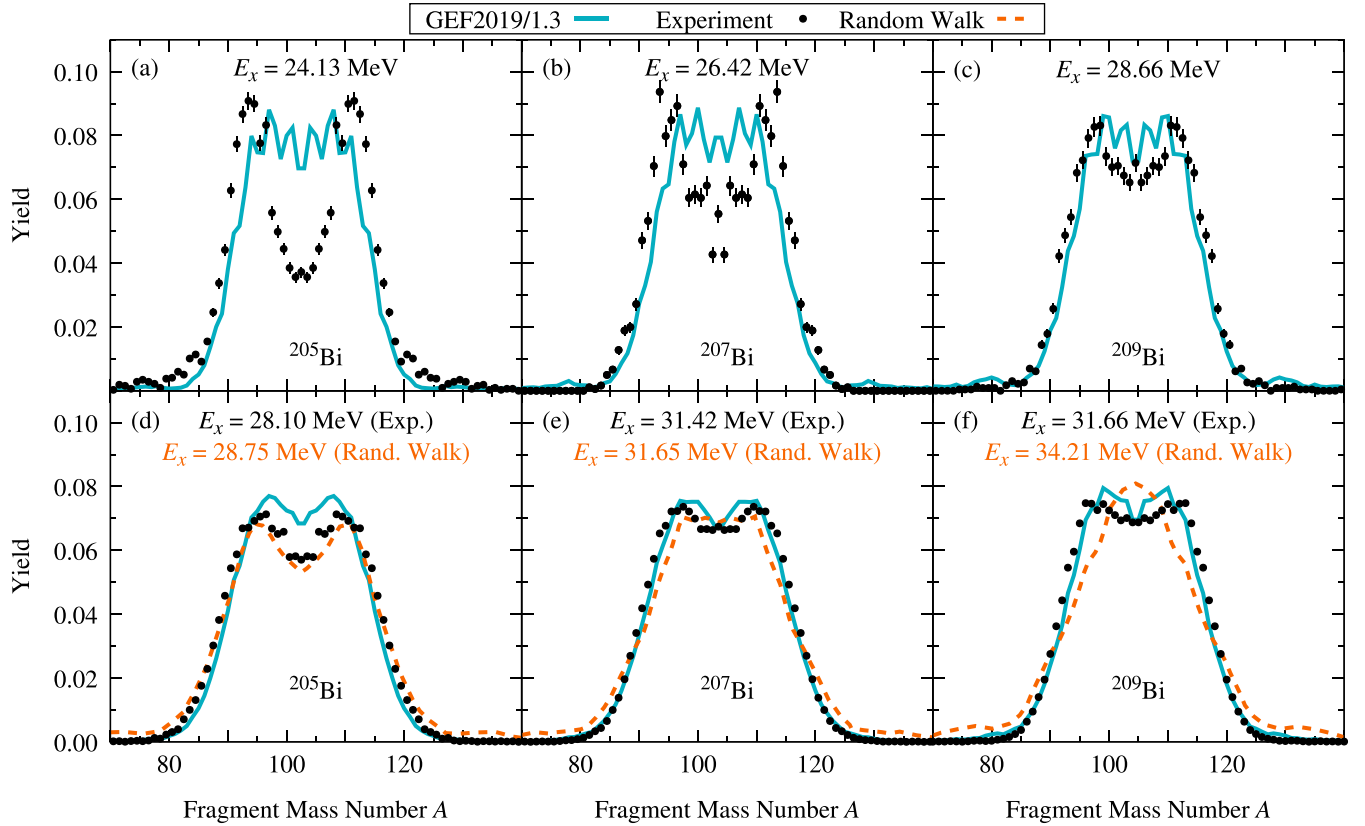


FIG. 10. (a)–(f) The measured fission fragment mass distributions for $^{205,207,209}\text{Bi}$ are compared to GEF2019/1.3 calculations (light blue lines). (d)–(f) Measured mass distributions are compared with the random-walk calculations over a potential-energy surface (PES), which are scanned from [33] and replotted. Note that while the excitation energies used in the random-walk calculations for $^{205,207}\text{Bi}$ are well matched to the experimental data, the excitation energy for ^{209}Bi is 2.55 MeV larger than the experimental data, which could contribute to the random-walk calculations showing a much narrower and more mass-symmetric mass distribution.

IV. CONCLUSIONS

Fission fragment mass distributions were determined for $^{205,207,209}\text{Bi}$ fission through proton bombardment of $^{204,206,208}\text{Pb}$, using a newly developed time difference analysis method. Previous measurements of $^{205,207}\text{Bi}$ fission mass distributions by Itkis *et al.* [15,16] are well reproduced, validating the analysis method developed in this paper.

The measured mass distributions of all three Bi isotopes exhibit a component of mass-asymmetric fission at all energies studied. Triple-Gaussian fits were used to extract the main characteristics of the mass-symmetric and mass-asymmetric fission modes. The fraction of the mass-asymmetric component decreases with increasing excitation energy from $\approx 70\%$ to $\approx 40\%$, which could be due to the reduction of shell effects, responsible for the asymmetric fission modes, with temperature. This could also be caused by the saddle point leading to the symmetric valley being higher than that for the asymmetric valley. In this case when the excitation energy is well above both barriers, each mode would be expected to contribute approximately equally. Comparisons between the three bismuth isotopes at similar excitation energies hint at an increase in the mass-symmetric fission yield with increasing neutron number, which supports the conclusion that there is a difference

between the fission barriers for the symmetric and asymmetric modes. The centroids of the mass-asymmetric peaks point towards the possible origin of the observed mass-asymmetric fission, where several deformed shell effects in the fission fragments could be contributing to the presence of the mass-asymmetric fission mode with predicted deformed shell gaps at $Z_{\text{light}} \simeq 38$ and $Z_{\text{heavy}} \simeq 45$ and $N_{\text{light}} \simeq 56$ all present in the fission fragments.

Comparison with GEF calculations shows good agreement at the highest excitation energies, but the GEF calculations fail to reproduce the trend of increasing mass-asymmetric fission fraction at lower excitation energies. This accentuates the need for fission measurements at excitation energies close to the fission barrier. Comparisons to random-walk calculations across a potential-energy surface show good agreement, but calculations are required at lower excitation energies to rigorously test this method, and other theoretical models.

Microscopic calculations of potential-energy surfaces would be useful to better understand the origin of the shell effects driving asymmetric fission in this region. Modern theoretical tools are now available to study both PES properties and the dynamical effects on fission (see [37,38] for recent reviews). It would be interesting to have fully microscopic predictions for the measurements presented in this paper.

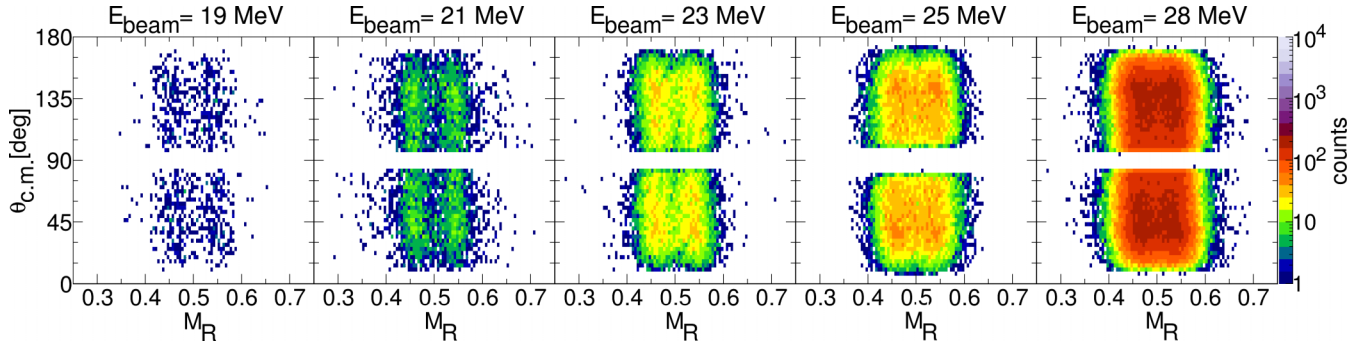


FIG. 11. Mass-angle distribution as a function of mass ratio, M_R , for 19-, 21-, 23-, 25-, and 28-MeV protons on ^{204}Pb . Approximately 400, 3000, 11 000, 20 000, and 97 000 fissions were observed, respectively. The plots display the number of fission fragments, which is twice the number of fission events detected.

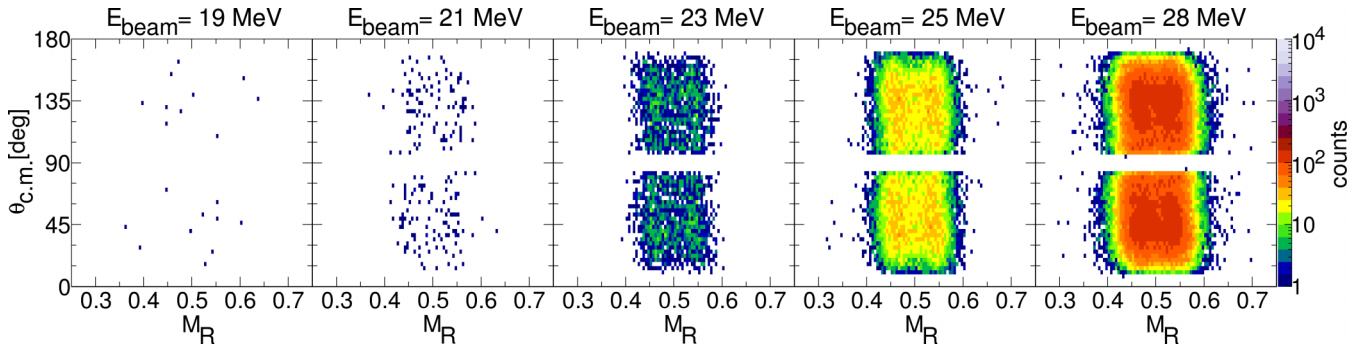


FIG. 12. As in Fig. 11 but for 19-, 21-, 23-, 25-, and 28-MeV protons on ^{206}Pb . Approximately 10, 100, 1800, 14 000, and 63 000 fissions were observed, respectively.

TABLE IV. Triple-Gaussian fit parameters determined in this paper following the methods described in the text.

Isotope	E_x (MeV)	σ_{sym}	σ_{asym}	A_{light}	A_{heavy}	Symmetric fission fraction
^{205}Bi	22.13	8.15 ^a	3.8(7)	93.6(7)	111.4(7)	0.28(14)
^{205}Bi	24.13	8.30 ^a	3.40(13)	93.34(13)	111.66(13)	0.35(2)
^{205}Bi	26.11	8.36(14)	3.91(13)	93.67(17)	111.33(17)	0.42(3)
^{205}Bi	28.11	8.63(17)	5.0(3)	93.6(4)	111.4(4)	0.43(6)
^{205}Bi	31.10	8.70(6)	4.78(13)	93.6(2)	111.4(2)	0.57(2)
^{207}Bi	24.44	6.30 ^a	3(1)	95(13)	112(13)	0.30(14)
^{207}Bi	26.42	6.90 ^a	3.8(3)	94.4(3)	112.6(3)	0.38(5)
^{207}Bi	28.42	7.51(13)	3.94(10)	94.36(13)	112.63(13)	0.481(18)
^{207}Bi	31.42	8.16(6)	4.29(9)	94.21(13)	112.79(13)	0.603(13)
^{209}Bi	28.66	7.10 ^a	3.8(3)	95.7(4)	113.3(4)	0.55(4)
^{209}Bi	31.66	7.70(8)	3.93(11)	95.16(14)	113.84(14)	0.623(14)

^aFixed symmetric widths (see text).

This paper has highlighted the importance of measuring fission mass distributions close to the fission barrier, which give clearer insights into the competition between the mass-asymmetric and mass-symmetric fission modes. Further systematic measurements at these energies for a range of different nuclei in this mass region will provide thorough tests of new models of nuclear fission.

ACKNOWLEDGMENTS

The authors acknowledge support from the Australian Research Council through Discovery Grants No. DP170102318, No. DP170102423, No. DP190100256, and No. DP200100601. This work was performed under the auspices of the U.S. Department of Energy by Lawrence Livermore National Laboratory under Contract No. DE-AC52-07NA27344. Support for the ANU Heavy Ion Accelerator Facility operations from the Australian National Collaborative Research Infrastructure Strategy (NCRIS) HIA project is acknowledged. B.M.A.S.-B., J.B., L.T.B., and K.V.-P. acknowledge the support of the Australian Government Research Training Program.

APPENDIX A: EXPERIMENTAL MASS-ANGLE DISTRIBUTIONS

Experimental MADs, which show the distribution of fission fragment mass ratio as a function of center-of-mass

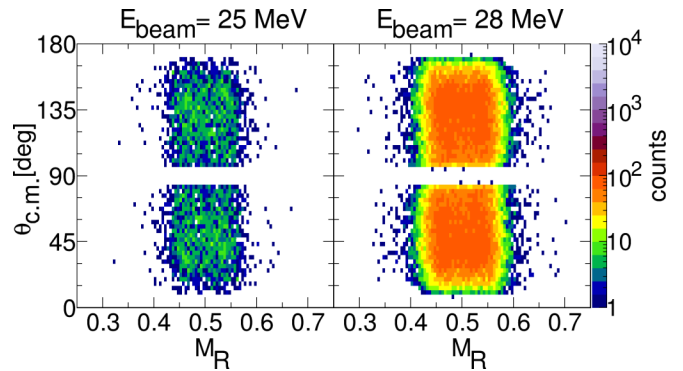


FIG. 13. As in Fig. 11 but for 25- and 28-MeV protons on ^{208}Pb . Approximately 2200 and 40 000 fissions were observed, respectively.

scattering angle, $\theta_{c.m.}$, were used to extract all mass distributions presented in this paper. For completeness, measured MADs for each target at selected beam energies are presented in Figs. 11, 12, and 13. The MADs highlight the wide angular coverage of the MWPCs and also the number of fissions measured for each reaction. The mass ratio being independent of angle confirms the correctness of the analysis procedures used in this paper.

APPENDIX B: TRIPLE-GAUSSIAN FIT PARAMETERS

The fit parameters for all triple-Gaussian fits are presented in Table IV.

-
- [1] L. Meitner and O. R. Frisch, *Nature (London)* **143**, 239 (1939).
 - [2] O. Hahn and F. Strassmann, *Naturwissenschaften* **27**, 11 (1939).
 - [3] A. Andreyev, K. Nishio, and K.-H. Schmidt, *Rep. Prog. Phys.* **81**, 016301 (2017).
 - [4] K.-H. Schmidt and B. Jurado, *Rep. Prog. Phys.* **81**, 106301 (2018).
 - [5] N. Bohr and J. A. Wheeler, *Phys. Rev.* **56**, 426 (1939).
 - [6] L. Meitner, *Nature (London)* **165**, 561 (1950).
 - [7] R. Vandenbosch and J. R. Huizenga, *Nuclear Fission* (Academic Press, New York, 1973).
 - [8] K.-H. Schmidt, S. Steinhäuser, C. Böckstiegel, A. Grewe, A. Heinz, A. R. Junghans, J. Benlliure, H.-G. Clerc, M. De Jong, J. Müller, M. Pfützner, and B. Voss, *Nucl. Phys. A* **665**, 221 (2000).
 - [9] C. Böckstiegel, S. Steinhäuser, K.-H. Schmidt, H.-G. Clerc, A. Grewe, A. Heinz, M. de Jong, A. R. Junghans, J. Müller, and B. Voss, *Nucl. Phys. A* **802**, 12 (2008).
 - [10] G. Scamps and C. Simenel, *Nature (London)* **564**, 382 (2018).
 - [11] A. N. Andreyev, J. Elseviers, M. Huyse, P. Van Duppen, S. Antalic, A. Barzakh, N. Bree, T. E. Cocolios, V. F. Comas, J. Diriken, D. Fedorov, V. Fedosseev, S. Franchoo, J. A. Heredia, O. Ivanov, U. Köster, B. A. Marsh, K. Nishio, R. D. Page, N. Patronis, M. Seliverstov, I. Tsekhanovich, P. Van den Bergh, J. Van De Walle, M. Venhart, S. Vermote, M. Veselsky, C. Wagemans, T. Ichikawa, A. Iwamoto, P. Möller, and A. J. Sierk, *Phys. Rev. Lett.* **105**, 252502 (2010).
 - [12] I. Tsekhanovich, A. N. Andreyev, K. Nishio, D. Denis-Petit, K. Hirose, H. Makii, Z. Matheson, K. Morimoto, K. Morita, W. Nazarewicz, R. Orlandi, J. Sadhukan, T. Tanaka, M. Vermeulen, and M. Warda, *Phys. Lett. B* **790**, 583 (2019).
 - [13] G. Scamps and C. Simenel, *Phys. Rev. C* **100**, 041602(R) (2019).
 - [14] M. G. Itkis, N. A. Kondratev, S. I. Mulgin, V. N. Okolovich, A. Y. Rusanov, and G. N. Smirenkin, *Yad. Fiz.* **52**, 944 (1990).
 - [15] M. G. Itkis, V. N. Okolovich, and G. N. Smirenkin, *Nucl. Phys. A* **502**, 243 (1989).
 - [16] M. G. Itkis, V. N. Okolovich, A. Y. Rusanov, and G. N. Smirenkin, *Sov. J. Nucl. Phys.* **41**, 544 (1985).
 - [17] R. H. Spear, D. C. Kean, M. T. Esat, A. M. R. Joye, and M. P. Fewell, *Nucl. Instrum. Methods* **147**, 455 (1977).
 - [18] P. Möller, A. J. Sierk, T. Ichikawa, A. Iwamoto, and M. Mumpower, *Phys. Rev. C* **91**, 024310 (2015).
 - [19] R. du Rietz, E. Williams, D. J. Hinde, M. Dasgupta, M. Evers, C. J. Lin, D. H. Luong, C. Simenel, and A. Wakhle, *Phys. Rev. C* **88**, 054618 (2013).
 - [20] D. J. Hinde, M. Dasgupta, J. R. Leigh, J. C. Mein, C. R. Morton, J. O. Newton, and H. Timmers, *Phys. Rev. C* **53**, 1290 (1996).

- [21] E. Williams, D. J. Hinde, M. Dasgupta, R. du Rietz, I. P. Carter, M. Evers, D. H. Luong, S. D. McNeil, D. C. Rafferty, K. Ramachandran, and A. Wakhle, *Phys. Rev. C* **88**, 034611 (2013).
- [22] J. Töke, R. Bock, G. X. Dai, A. Gobbi, S. Gralla, K. D. Hildenbrand, J. Kuzminski, W. F. J. Müller, A. Olmi, H. Stelzer, B. B. Back, and S. Bjørnholm, *Nucl. Phys. A* **440**, 327 (1985).
- [23] R. K. Choudhury, A. Saxena, A. Chatterjee, D. V. Shetty, S. S. Kapoor, M. Cinausero, L. Corradi, E. Farnea, E. Fioretto, A. Gadea, D. Napoli, G. Prete, A. M. Stefanini, D. Bazzaco, S. Beghini, D. Fabris, G. Montagnoli, G. Nebbia, C. Rossi-Alvarez, F. Scarlassara, C. Ur, and G. Viesti, *Phys. Rev. C* **60**, 054609 (1999).
- [24] R. G. Thomas, D. J. Hinde, D. Duniec, F. Zenke, M. Dasgupta, M. L. Brown, M. Evers, L. R. Gasques, M. D. Rodriguez, and A. Diaz-Torres, *Phys. Rev. C* **77**, 034610 (2008).
- [25] P. Glässel, D. v. Harrach, H. J. Specht, and L. Grodzins, *Z. Phys. A* **310**, 189 (1983).
- [26] J. C. Gehring, B. B. Back, R. R. Betts, P. B. Fernandez, D. J. Henderson, and Y. Nagame, *Phys. Rev. C* **44**, R1(R) (1991).
- [27] V. E. Viola, K. Kwiatkowski, and M. Walker, *Phys. Rev. C* **31**, 1550 (1985).
- [28] J. D. McDonnell, W. Nazarewicz, J. A. Sheikh, A. Staszczak, and M. Warda, *Phys. Rev. C* **90**, 021302(R) (2014).
- [29] F. A. Ivanyuk, C. Ishizuka, M. D. Usang, and S. Chiba, *Phys. Rev. C* **97**, 054331 (2018).
- [30] A. Ignatyuk, G. Smirenkin, and A. Tishin, *Yad. Fiz.* **21**, 485 (1975).
- [31] A. O. Macchiavelli, J. Burde, R. M. Diamond, C. W. Beausang, M. A. Deleplanque, R. J. McDonald, F. S. Stephens, and J. E. Draper, *Phys. Rev. C* **38**, 1088 (1988).
- [32] K. Mahata, C. Schmitt, S. Gupta, A. Shrivastava, G. Scamps, and K.-H. Schmidt, [arXiv:2007.16184](https://arxiv.org/abs/2007.16184).
- [33] P. Möller and J. Randrup, *Phys. Rev. C* **91**, 044316 (2015).
- [34] K.-H. Schmidt, B. Jurado, C. Amouroux, and C. Schmitt, *Nucl. Data Sheets* **131**, 107 (2016).
- [35] J. Randrup and P. Möller, *Phys. Rev. C* **88**, 064606 (2013).
- [36] A. Bulgac, S. Jin, K. J. Roche, N. Schunck, and I. Stetcu, *Phys. Rev. C* **100**, 034615 (2019).
- [37] N. Schunck and L. M. Robledo, *Rep. Prog. Phys.* **79**, 116301 (2016).
- [38] C. Simenel and A. Umar, *Prog. Part. Nucl. Phys.* **103**, 19 (2018).